# Extreme Scintillation Structure Diagnostics

- <sup>2</sup> Charles Rino<sup>a,1\*</sup>, Charles Carrano<sup>a</sup>, Dmytro Vasylyev<sup>c</sup>, Luca Spogli<sup>d</sup>, Theodore Beach<sup>a</sup>,
- 3 Yu Morton<sup>b</sup> and Keith Groves<sup>a</sup>
- <sup>4</sup> Institute for Scientific Research, Boston College, Massachusetts, USA
- b University of Colorado, Boulder, Colorado, USA
- <sup>6</sup> Institute for Solar-Terrestrial Physics, German Aerospace Center, Neustrelitz, Germany
- <sup>d</sup>National Institute of Geophysics and Vulcanology, Rome, Italy

#### ARTICLE INFO

# Keywords:

1 A

12

14

16

1.8

19

20

21

22

27

29

32

33

37

38

41

42

43

47

48

- 13 Ionosphere
  - GNSS Scintillation
- 15 Equatorial Plasma Bubbles
  - Backpropagation

#### ARTICLE IIVI O

#### ABSTRACT

Satellite constellations that comprise the global navigation satellite system are monitoring the ionosphere routinely for space-weather forecasting. However, diagnostic structure analysis has been confined to dedicated studies. This paper demonstrates a new diagnostic procedure that exploits back propagation (BP) to reduce scintillation that evolves as signals propagate through the disturbed ionosphere and free space. BP has been used primarily to localize structure imposed during ionosphere occultation. However, BP can be applied more broadly to satellite-to near-earth observations. The new approach applies irregularity parameter estimation (IPE) to phase extracted after BP.

BP-IPE applications to low-latitude strong scintillation data are presented, which reveal new structure characteristics distinctly different from commonly measured structure associated with equatorial plasma bubbles. The procedures are validated with multiple phase screen simulations.

## 1. Introduction

Scintillation is formally a stochastic modulation imparted to an electromagnetic (EM) field as it propagates through a structured medium. A companion paper reviewed diagnostic applications of a two-dimensional propagation theory based on a phase screen model [1]. The phase-screen theory is strictly valid only for fields initiated by a phase screen followed by free-space propagation. However, it has been demonstrated that multiple-phase-screen (MPS) simulations of propagation through extended regions produce results that are statistically equivalent to fields generated by path-integrated phase screens placed at the center of the disturbed regions [2]. Moreover, MPS simulations are very effective for characterizing satellite-to-near-earth propagation. Examples include direct model reconciliation of diagnostic measurements [3], propagation through measured structure [4], and propagation through simulated structure [5].

Irregularity parameter estimation (IPE) is a formal procedure for constructing parameter estimates that reconcile parameterized theoretical predictions with measurements. IPE is most effective when applied to a stochastic process that supports a defining spectral density function (SDF) [6]. The theory of propagation in random media is encapsulated in a hierarchy of differential equations that can be solved for complex field moments with structure characterized by path-integrated phase structure functions [7]. An algorithmic implementation of the intensity SDF for a phase screen has been used successfully for IPE parameter estimation of both structure parameters and the propagation distance [8]. IPE has also been applied successfully to total electron content (TEC) residuals as a direct measure of path-integrated phase structure [9]. However, computational complexity and susceptibility to diffraction effects have limited diagnostic IPE applications to dedicated observations.

Back propagation (BP), which can remove or reduce propagation-induced scintillation, has been used mainly to estimate the location of intercepted occultation GPS structure [10]. However, whereas the occultation path structure location is unknown a-priori, for conventional satellite-to-near-earth propagation paths the ionosphere penetration point at a specified height provides a an estimate of the location of the disturbed region. In that case the BP reduction of scintillation structure following propagation from the penetration point can be exploited further as demonstrated by Breitsch and Morton [11]. This paper extends the use of BP to construct an equivalent phase-screen field, which is then used to extract the path-integrated phase to which IPE can be applied directly. BP-IPE provides an estimate of

<sup>\*</sup>Corresponding author ORCID(s):

the propagation distance and the structure parameters without intermediate theoretical results. The procedure is robust and computationally efficient.

MPS simulations are used to validate diagnostic applications of BP-IPE. MPS simulations are restricted only by the narrow propagation angle range of the supporting plane-wave field components. Results from applying BP-IPE structure estimation to data from a one year GPS campaign designed to capture extreme scintillation for processor evaluation are summarized. Applications to more recent GNSS data collected during recent coronal mass ejection events are also summarized.

## 2. BP Diagnostic Processing

Following the development in [1], the complex field measured at a point in a forward propagation plane can be modeled by a homogeneous stochastic process embedded in a background of white noise. Scintillation is caused by intermediate scale structure spanning tens of kilometers to hundreds of meters, which evolve slowly enough by be considered frozen over measurement intervals. Space-time structure translation is realized with an effective scan velocity, which depends on the propagation direction, the magnetic field direction, anisotropy coefficients, the motion of the coordinate system reference point, and the structure drift. Allowing for striation along magnetic field lines, 2D stochastic variation is captured by projecting the striations onto cross-field slice planes that contain the propagation path. A large body of mid-to-low-latitude diagnostic measurements are amenable to characterization by 2D propagation in slice planes that intersect the elongated field structure.

To interpret the processing operations let  $\Delta N_e(x, y)$  represent the projected 2D structure intercepting the propagation plane. The 3D spectral density function (SDF),

$$\Phi_{\Delta N_e}(\kappa_s) = C_s \left\{ \begin{array}{c} \kappa_s^{-\eta_1}, \, \kappa_s \leq \kappa_0 \\ (\kappa_0^{\eta_2 - \eta_1}) \kappa_s^{-\eta_2}, \, \kappa_s > \kappa_0 \end{array} \right. , \tag{1}$$

where  $\kappa_s$  is the magnitude of the 3D spatial wave number, was introduced in [12]. The 2D *SDF* that characterizes  $\Delta N_e(x,y)$  can be derived from (1) with a coordinate rotation about the magnetic field direction followed by an integration as described in [12]. Propagation theory is functionally dependent on electron density via a path integration.

In the two-dimension plane

$$\phi(y) = 2\pi K/f \int_0^L \Delta N_e(x, y) dx. \tag{2}$$

The factor

51

5.2

53

54

55

56

5.7

59

60

61

62

66

67

$$K = r_o c / (2\pi) \times 10^{16},\tag{3}$$

where f represents frequency,  $r_e = 2.819740289 \times 10^{-15}$  m is the classical electron radius, and c is the vacuum velocity of light converts TEC to phase units. The parameter L is a layer thickness measure. The SDF of the projected pathintegrated phase can be computed directly from (2) as

$$\Phi_{\phi}(\kappa_{y}) = (2\pi K L/f)^{2} \int \frac{\sin^{2}\left(\kappa_{x} L/2\right)}{\left(\kappa_{x} L/2\right)^{2}} \Phi_{\Delta N_{e}}(\kappa_{x}, \kappa_{y}) \frac{d\kappa_{x}}{2\pi},\tag{4}$$

where  $\Phi_{\Delta N_e}(\kappa_x, \kappa_y)$  is the 2D SDF in the xy coordinate system. Allowing for decorrelation along the propagation path, the following approximation can be used:

$$\Phi_{\phi}(\kappa_y) = (2\pi K/f)^2 L \Phi_{\Delta N_e}(0, \kappa_y). \tag{5}$$

For diagnostic measurements we let

$$\Phi_{\phi}(\kappa_{y}) = C_{p} \left\{ \begin{array}{c} \kappa_{y}^{-p_{1}}, \kappa_{y} \leq \kappa_{0} \\ (\kappa_{0}^{p_{2}-p_{1}})\kappa_{y}^{-p_{2}}, \kappa_{y} > \kappa_{0} \end{array} \right.$$
 (6)

Time-to-space conversion factors are absorbed in  $C_p$ . Over the power-law range the radial wavenumber index  $\eta$  is related to the corresponding one-dimensional SDF index as  $p = \eta + 1$ . Stochastic realizations of  $\phi(y)$  completely

define the MPS interaction of an initiating field with an extended ionospheric region. Free-space propagation over a distance  $\Delta x$  is defined by the operation

$$\psi(x \pm \Delta x, y) = \int \widehat{\psi}(\kappa_y; x) \left[ \exp\{\mp i \left( \sqrt{1 - \left( \kappa_y / k \right)^2} - 1 \right) \left( k \rho_F \right)^2 \} \right]$$

$$\times \exp\{i \kappa_y y\} d\kappa_y / (2\pi),$$
(7)

where  $k = 2\pi f_c/c$ ,  $\rho_F = \sqrt{\Delta x/k}$  is the Fresnel scale, and

$$\widehat{\psi}(\kappa_y; x) = \int \psi(x, y) \exp\{-i\kappa_y y\} dy \tag{8}$$

is the y Fourier transform of the complex field  $\psi(x, y)$ . Defining the propagation step as  $\Delta x = k\rho_F^2$  anticipates the narrow-propagation-angle constraint,  $(\kappa_y/k)^2 \ll 1$ . The phase modification in square brackets takes the simpler form  $\exp\{\pm i \left(\kappa_y \rho_F\right)^2/2\}$ , which implies equivalent scintillation at distances and frequencies that preserve  $\rho_F$ . Detrending operations constrain the largest contributing measurement scales, which define locally homogeneous segments over which the summarized relations apply.

Forward propagation for MPS simulation uses the upper sign. Back propagation uses the lower sign. Back propagation is initiated with the measured field nominally at the propagation distance from the ionosphere penetration point. Nelder-Mede minimization [13] is applied to  $\langle |\psi(x \pm \Delta x, y)|^2 \rangle$ . If a minimum corresponding to S4 < 1 is realized, the field  $\psi(x - \Delta x, y)$  is accepted as an estimate of the field initiating free-space propagation. If no minimum is found or the minimum S4 exceeds unity, BP to the distance from the penetration point is accepted as the field initiating free-space propagation. The phase of the initiating field is extracted with a standard unwrapping algorithm IPE as described in [9] is applied to the periodogram of the reconstructed phase.

## 2.1. MPS BP Simulation

The following procedure is used to generate sampled phase realizations:

$$\phi(n\Delta y) = \sum_{m=0}^{N-1} \sqrt{\Phi_{\phi}(m\Delta\kappa_y)\Delta\kappa_y/(2\pi)} \eta_m \exp\{2\pi nm/N\}$$
(9)

where  $\eta_k$  is a sequence of uncorrelated unit variance complex random variables. Formally,

$$\langle \eta_k \eta_{k'}^* \rangle = \delta(k - k'),$$
 (10)

where  $\delta(k)$  is the Kronecker delta function. From the FFT operation

$$\widehat{\phi}(m\Delta\kappa) = \frac{1}{N} \sum_{n=0}^{N-1} \phi(n\Delta y) \exp\{-2\pi i n m/N\},\tag{11}$$

it follows that

88

89

90

91

92

93

96

97

104

105

106

107

108

109

$$\left\langle \left| \hat{\phi}(m\Delta\kappa) \right|^2 \right\rangle = \Phi_{\phi}(m\Delta\kappa). \tag{12}$$

The summations are implemented with fast Fourier transforms (FFTs) sampled from  $\pm \Delta \kappa$  to  $\pm N \Delta \kappa / 2$  where  $\Delta \kappa = 2\pi / N$  and  $\Delta \kappa = 2\pi / (N \Delta y)$ . A  $\Delta \kappa_v / (2\pi)$  scaling preserves the Parseval relation

$$\left\langle \frac{1}{N} \sum_{n=0}^{N-1} |\phi(n\Delta y)|^2 \right\rangle = \sum_{m=0}^{N-1} \Phi_{\phi}(m\Delta \kappa_y) \Delta \kappa_y / (2\pi). \tag{13}$$

For notational efficiency the continuous forms of the functional relations will be used with FFT evaluation implied. MPS starts with an initiating complex field. A phase realization is used to impose a phase perturbation. The modified field is propagated over an incremental distance, typically several hundred wavelengths. Exact propagation defined by (7) suppresses small-scale structure with  $\kappa_y < k$ , although local wavelength-scale structure can be produced, e. g. caustics. Free propagation is implemented incrementally to avoid phase discontinuities. The spatial frequency extent of the evolving PSD is a check on the small propagation angle constraint.

## 2.2. Diagnostic Measures

Diagnostic measures are applied to time series. We assume that the complex field reconstructed from intensity and phase measurements is an ideal representation of the detected complex field unaffected by noise, multipath, interference, and limitations of the detection operations. Conversion from spatial simulation coordinates to time is achieved with an effective scan velocity such that  $y = v_{\text{eff}}t$ . For interpreting data  $v_{\text{eff}}$  at a height-dependent ionospheric penetration can be computed from the known propagation and magnetic field directions and the penetration velocity corrected for structure motion. For simulations, representative  $v_{\text{eff}}$  values are used. Upon space-to-time translation the simulated complex fields are represented as

$$\psi(t) = \sqrt{I(t)} \exp\{i\phi(t)\},\tag{14}$$

118 where

111

112

113

114

115

116

117

121

$$I(t) = |\psi(x, t)|^2$$
. (15)

Exact recovery of phase from a complex field requires sampling that can resolve phase changes smaller than  $\pi$  radians. Extracting phase from detected signals requires phase tracking and phase jump correction.

Standard diagnostic measures include the intensity scintillation index

$$S4 = \sqrt{\langle I(t)^2 \rangle / \langle I(t) \rangle^2 - 1},\tag{16}$$

122 rms phase

$$\sigma_{\phi} = \sqrt{\langle \phi(t)^2 \rangle - \langle \phi(t) \rangle^2},\tag{17}$$

and the rate of change of TEC

$$ROTI(\Delta T) = \sqrt{\langle (\Delta T E C(t) - \Delta T E C(t + \Delta T))^2 \rangle / \Delta T},$$
(18)

124 where

$$SFN(\Delta T) = \langle (\Delta T EC(t) - \Delta T EC(t + \Delta T))^2 \rangle$$
(19)

defines a structure function. The notation  $\Delta TEC(t)$  denotes a residual after removal of large-scale structure. Upon neglecting the scintillation-dependent residual from geometric-Doppler-free combinations,  $\phi(t)$  and TEC(t) are related by the frequency-dependent scale factor in (2). We assume that  $\psi(t)$  and  $I(t) = |\psi(t)|^2$  have well-defined spectral density functions denoted  $\Phi_{\psi}(f)$  and  $\Phi_{I}(f)$  respectively. The mutual coherence function

$$MCF(\Delta T) = \langle \psi(t)\psi^*(t + \Delta T) \rangle,$$

is a measure of temporal coherence related to  $\Phi_{\psi}(f)$  via the Fourier transformation

$$MCF(\Delta T) = \int \Phi_{\psi}(f) \exp\{2\pi i f \Delta T\} df. \tag{20}$$

The standard diagnostic measures are evaluated with sample moments. Spectral density functions are evaluated with periodogams. The following relations provide consistency checks

$$S4^{2} = \int \Phi_{I}(f)df + 1, \tag{21}$$

132 and

$$\langle I(t)^2 \rangle = \int \Phi_{\psi}(f) df.$$
 (22)

## 3. BP-IPE Simulations

Diagnostic GNSS receivers typically provide 50 or 100 Hz intensity and phase data samples at L-band frequencies. The primary frequencies used for TEC computation are designated L1 and L2. MPS simulations are initiated with a narrow-beam starting field. Critically sampled ( $\Delta y = \lambda/2$ ) phase realizations are used to generate phase perturbations followed by free propagation using (7) with  $\Delta x = 600\lambda$ . Sensitivity to structure parameters was demonstrated in the companion publication [1]. From the BP-IPE analysis summarized in Section 4 below we find two distinct structure classes, namely equatorial plasma bubble structure with p1 < p2, denoted EPB referring to equatorial plasma bubbles and asecond structure class with p1 > p2, designated PPB referring to prominent plasma bubbles with p1 > p2. Our objective is to demonstrate that BP-IPE processing generates structure parameter estimates that distinguish the two structure classes under observed moderate to extreme scintillation conditions. Representative p1, p2, and  $\kappa_0$  values were chosen with  $C_p$  adjusted to generate moderate EPB L2 scintillation and stronger L2 PPB scintillation. The L2 frequency (1227.6 MHz) was chosen as the smallest frequency common to GNSS constellation TEC measurements.

Realizations were initiated using 50-km phase screens with  $v_{\rm eff}$  chosen to generate 100-Hz realizations spanning 5-min segments. MPS was applied over 40 km followed by free propagation to 142 km. Figures 1 and 2 summarize the intensity and phase at 142 km from 12 concatenated 5-min realizations of the representative EPB and PPB structures. Green pentagrams locate the centers of each 5-min segment. Phase was extracted from the complex field realizations using conventional unwrapping. The linear phase variation was removed to avoid phase discontinuities at the segment transitions. The figure titles list the defining spatial-domain structure parameters.

S4 and  $\sigma_{\phi}$  indices were computed over each 5-min segment using sample moments. For completeness the standard deviation of the phase difference  $(\phi(t) - \phi(t + \Delta T))/\Delta T$  was computed with  $\Delta T = 1$  min and reported as ROTI in radians. The calculation is an implementation of method 1 described in [14], but applied to single-frequency phase differences. The results are summarized in the following tables:

**EPB** 

Diagnostic	mean	std
<i>S</i> 4	0.84	0.03
$\sigma_{\phi}$	12.65 rad	3.38 rad
ROTI – 1min	0.19 rad	0.08 rad

#### **PPB**

Diagnostic	mean	std
<i>S</i> 4	1.00	0.01
$\sigma_{\phi}$	87.30 rad	33.90 rad
ROTI – 1min	0.94 rad	0.44 rad

The summary parameters reflect the very large change in phase structure from EPB to PPB. However, because S4 ultimately saturates at a value approaching one, the summary parameters provide no direct indication of the coherence reduction prominent in the upper frames of Figures 1 and 2.

The upper left frames in Figures 3 and 4 show the first segment S4 evolution with MPS (red) and free space (blue) identified. The upper right frames show the intensity at 142 km, which is repeated for reference from the upper frames of Figures 1 and 2. Green pentagrams mark the BP S4 values at the propagation distance to the reported minimum variance distance. The lower left frames show the initiating phase (blue circles) and the extracted BP phase (red line). The lower right frames show the difference between the initiating and BP phase. The PPB realizations reach saturation before free-space propagation. However, a true BP minimum was found within the disturbed region even though the BP minimum S4 remained near unity. BP reduces S4 to small values only when the structure evolved from a phase screen with little or no amplitude variation followed by free space propagation.

Figures 5 and 6 summarize the BP-IPE structure parameters extracted from each 5-min segment. Consistent with the small EPB phase errors shown in the lower right frame of Figure 3, the initiating p1 and p2 parameters are recovered almost perfectly. Diffraction effects are confined to smaller scales, which are suppressed by BP. Only the initiating phase is strictly free of diffraction. The PPB parameters summarized in Figure 6 show more variability and larger p1 and p2 errors. However, the results show that the p1 and p2 order would be identified as PPB. Solid lines indicate the defining p1 and p2 values.

In summary the BP-IPE simulations show that very accurate structure parameter estimation is realized for EPB structure. Structure parameters from PPB segments have more variability but sustain PPB p1 > p2 classification. Regarding computational requirements, aside from preprocessing and detrending, which are common to all diagnostic procedures, BP-IPE is initiated with Fourier transforms followed by a rapidly convergent direct search minimization operation. No theoretical intermediaries are used. The calculations could be realized in near-real time.

## 4. GPS BP-IPE Diagnostics

21.0

The global positioning satellite (GPS) constellation satellites are deployed in 12-hr circular orbits configured to provide at least 4 favorably oriented satellites visible from any position on the earth's surface. Propagation through the ionosphere creates a delay that must be corrected but also provides an exceptional diagnostic capability. With support from internal funding from the University of Miami Prof. Jade Morton's laboratory designed and constructed a 25 MHz multi-frequency GPS data acquisition system, which was deployed in Hong Kong hosted by Prof. George Liu from Hong Kong Polytechnic University. The system was operated from October 2013 to July 2015 with data acquisition triggered by strong scintillation. Processed 100 Hz intensity and phase data were made available for this study. Following the intensity and phase processing operations summarized in [1] complex scintillation records were generated to support 5-min consecutive segments for BP-IPE processing. The 5-min processing intervals were needed to recover extreme scintillation structure. The Hong-Kong intensity and phase data will be made available upon request.

Figure 7 shows representative Hong Kong L1, L2, and L5 intensity data records converted to SNR units (blue) with mean intensity overlaid (red). The red circles locate centers of the 5-min segments. Detrended intensity is generated by normalizing the intensity to the mean. The left frame of Figure 8 summarizes S4 scintillation index estimates, which are evaluated over 5 min intervals offset by 2.5 min. The S4 variation within the 5-min processing segments indicates some inhomogeneity distortion of the intensity at the smallest frequencies.

The L2 and L5 frequencies are separated by 51 MHz, which is large enough to capture the frequency dependence of the S4 estimates. However, interference is evidently increasing the L5 intensity variation. Excluding the L5 data, the L1 and L2 estimates follow the expected frequency ordering with the exception of segments about 50-min where the frequency order is reversed. This is attributed to strong focusing. The lower frequency passes through strong focusing and followed by saturation while the higher frequency remains in strong focusing with a higher S4 value.

The left frames in Figure 9 summarize the Hong Kong scintillation with the expected higher occurrence of strong scintillation in the equinox periods. The right frame shows L1 and L2 occurrence distributions of  $\log_{10}(S4)$ . The distributions are consistent with the frequency dependence. A complex scintillation estimate is constructed by imposing the extracted phase after polynomial removal of a slowly varying component onto the detrended scintillation intensity. The identical BP minimization applied to the L2 simulations was applied to the Hong Kong L2 segments followed by phase extraction and IP processing to estimate the propagation distance and structure parameters. For theoretical comparison it is convenient to report the BP propagation distance as a Fresnel scale  $\rho_F = \sqrt{xBP/k}$ . Figure 10 summarizes the structure parameters after data editing to remove outliers. Of the surviving 1044 samples 504 were classified EPB and 540 were classified PPB. To emphasize two distinct structure types, the left and right frames summarize the EPB and PPB segments separately. The selected  $C_p$  values for simulation are within the measured BP-IPE range.

The measured structure parameters and propagation distance could used to compare the predicted and measured intensity spectral density. However, a more efficient check on the integrity of the IPE parameters is to verify that the independently measured S4 values are ordered by the universal strength parameter

$$U = C_P \begin{cases} \rho_F^{p_1 - 1} & \text{for } \mu_0 \le 1\\ \rho_F^{p_2 - 1} \kappa_0^{p_1 - p_2} & \text{for } \mu_0 \le 1 \end{cases} , \tag{23}$$

where  $\mu_0 = \kappa_0 \rho_F$ , [15]. The upper frames of Figure 11 show, respectively, S4 versus U scatter diagrams with U computed from (23) using the measured structure parameters. The S4 occurrence probabilities are shown in the lower frame. Here we see that extreme S4 values occur with EPB and PPB structures. However, PPB extreme S4 values are more likely. The population of small PPB S4 values may be a separate population of weak structure consistent with the two peaks shown in the lower frame of Figure 11. The simulations summarized in Section 2 show that IPE parameters are theoretically consistent with the EPB and PPB structure class identifications.

## 4.1. GNSS BP-IPE Diagnostic

25 2

Scintillation data managed by the Italian Istituto Nazionale di Geofisica e Vulcanologia (INGV) were utilized to complement the analysis. These data were collected by Ionospheric Scintillation Monitoring Receivers (ISMRs) situated in Lampedusa (Southern Italy), which covers the lower Western Mediterranean sector [16]. Additional data were collected from an ISMR receiver developed under the New Observatory for Real-time Ionospheric Sounding over Kenya (NORISK, https://norisk.rm.ingv.it/) project. The receiver is located at the Luigi Broglio Malindi Space Center in Kenya, which covers the southern crest of the equatorial ionospheric anomaly [17]. Both ISMRs are Septentrio PolaRx5S receivers, representing an advancement from the PolaRxS [18].

Data from the Luigi Broglio Malindi Space Center captured equatorial scintillation activity under conditions of high solar flux and equinox on 18-Mar-2019, while Lampedusa data captured the poleward expansion of equatorial plasma bubbles following the May 2024 Superstorm [19] on 10-May-2024.

ISMR data from Lampedusa and Malindi are available at www.eswua.ingv.it: https://doi.org/10.13127/ESWUA/GNSS Upper Atmosphere Physics and Radiopropagation Working Group: Electronic Space Weather Upper Atmosphere Database (eSWua)-GNSS Scintillation Data, Version 1.0. Istituto Nazionale di Geofisica e Vulcanologia (INGV) August 1, 2020.

Identical BP-IPE processing was applied to Malindi and Lampedusa 5-min L2 data segments sampled at 50 Hz. Figures 12 and 13 show strikingly similar extreme scintillation occurrence and distributions over two-day periods. Enhanced-to-extreme scintillation segments with

$$\log_{10}(S4 > 0.5) \ge -0.3$$

are confined to advancing or receding segments where equatorial plasma bubbles are intercepted. Figure 9 in Spogli et al. [19] summarizes the Lampedusa Gannon Storm activity. Regarding geometric sensitivity, all the disturbed segments intercept cross-field structure at elevation angles greater than 20 deg indicating that the enhancements are reflecting bubble structure rather than propagation geometry.

Figures 14 and 15 summarize the BP IPE parameters. Comparison to the right frame in Figure 10 show that dominant structure segments from Malandi and Lampedusa have almost exclusively PPB p1 > p2 characteristics. The second frame in each figure shows the power-law index difference p1 - p2. Nonnegative values identify PPB segments (red circles). The much smaller population of EPB signatures are identified with blue circles.

#### 5. Summary and Conclusions

Morphological studies of GNSS scintillation occurrence have been based mainly on S4,  $\sigma_{\phi}$ , and ROTI, diagnostics, which do not distinguish structure variations. Definitive structure diagnostics require dedicated processing operations with 50 Hz sampling or higher, which previously constrained applications to directed studies. However, expanding on diagnostic measurements that exploit BP, we have show that definitive structure diagnostics can be realized with efficient and robust computation procedures that do not rely on theoretical predictions from propagation theory.

Regarding expected structure characteristics, the two-component inverse-power-law structure with p1 < p2 was observed in early in-situ rocket measurement of equatorial plasma bubbles [20]. Analysis of in-situ satellite data from Atmospheric Explorer E [21] and C/NOFS [22] confirmed the EPB structure. Additionally, the frequency dependence implied by the EPB structure reconciled the unexpected occurrence of communication system S-Band scintillation [23, 24]. Further support came from physics-based high-resolution simulations of the dynamic evolution of equatorial plasma bubbles [25]. An EPB signature was derived from the simulation of an isolated F-layer plasma bubble. The isolated EPB structure is established when the plasma bubble penetrates F-region peak density. An evolving break-scale separating the p1 and p2 spatial frequencies was associated with the initiating bifurcation scale and evolution. Late phase structure approaches a single power law [See Figures 3 through 6 in [26]]. However, aside from the Hong Kong data presented in this paper, evidently there has been no exploration of structure variation associated with equatorial spread F. In our earlier studies using the same Hong Kong data [27] the association of PPB structure with extreme scintillation was put aside as a diffraction effect.

In light of the simulations in Section 3 we conclude that that BP-IPE processing is identifying segments with EPB and PPB structure. Indeed, the Hong Kong data analysis produced nearly equal numbers of EPB and PPB segments. Definitive EPB structure may be confined to isolated bubbles, whereas sustaining the PPB p1 > p2 as a variant of the gradient-drift instability evidently requires a different  $E \times B$  and background electron density profile. The similarity of

the Hong Kong and Malindi/Lampedusa PPB segments indicates that the generating process is not unique to extreme scintillation ( $S4 \sim 1$ ) is present in both EPB and PBP populations.

Evidence of  $E \times B$  driver and background electron density variations is discussed in a summary of the Lampedusa data acquired during the Gannon storm [See Figure 7 in [19]]. Additional analysis from operational equatorial stations should clarify the occurrence and conditions that produce EPB and PPB structure.

The main objectives of this paper were to introduce and validate a new analysis procedure that can provide definitive structure diagnostics. The preliminary results presented in this paper indicates that Equatorial Spread F can support different structure characteristics. Understanding of the physical processes that are causing the structure development should enhance our understanding of the process.

## 6. Aknowledgement

The authors thank Claudio Cesaroni and Emanuele Pica for their help with the ISMR data from Lampedusa and in Malindi. The ISMR in Malindi has been established as part of the New Observatory for Real-time Ionospheric Sounding over Kenya (NORISK, https://norisk.rm.ingv.it/) project, carried out in the framework agreement between the Italian Space Agency (ASI) and the Istituto Nazionale di Geofisica e Vulcanologia (INGV).

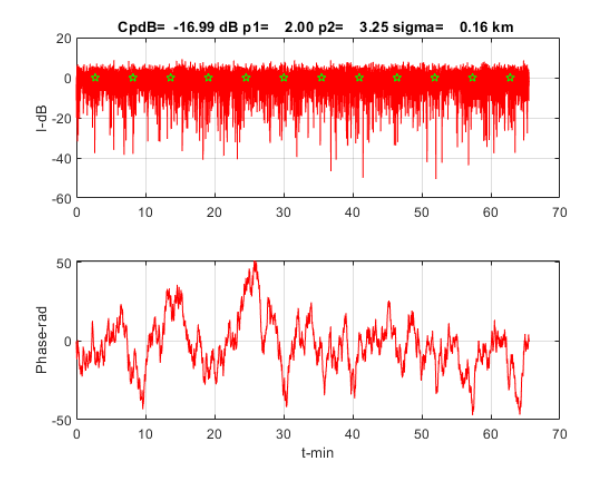


Figure 1: EPB Intensity and phase at 142 km.

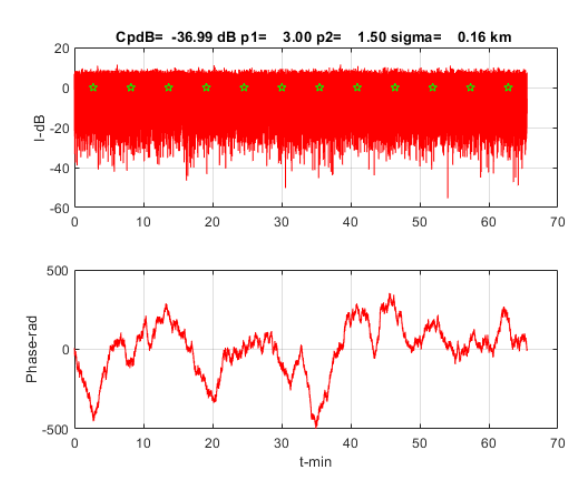


Figure 2: PPB Intensity and phase at 142 km.

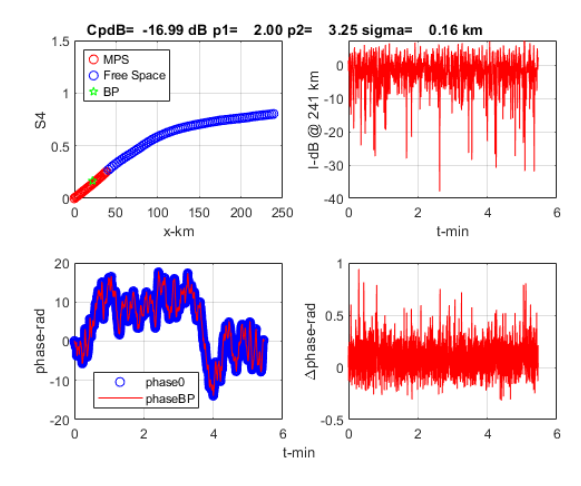


Figure 3: EPB segment 1 summary. Upper frames show S4 evolution and observation plane intensity. Lower frames compare initiating phase and recovered BP phase.

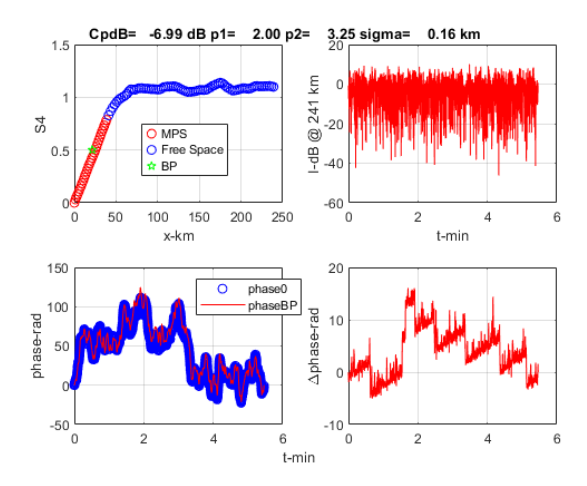


Figure 4: PPB segment 1 summary. Upper frames show S4 evolution and observation plane intensity. Lower frames compare initiating phase and recovered BP phase.

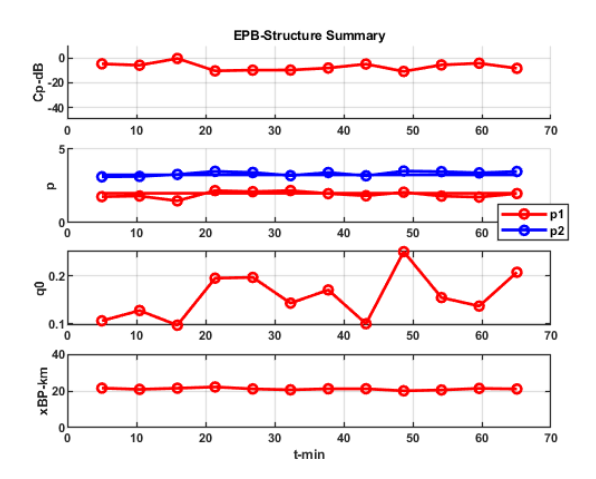


Figure 5: Summary of measured EPB structure parameters. Straignt blue and red lines blue indicate initiate true values.

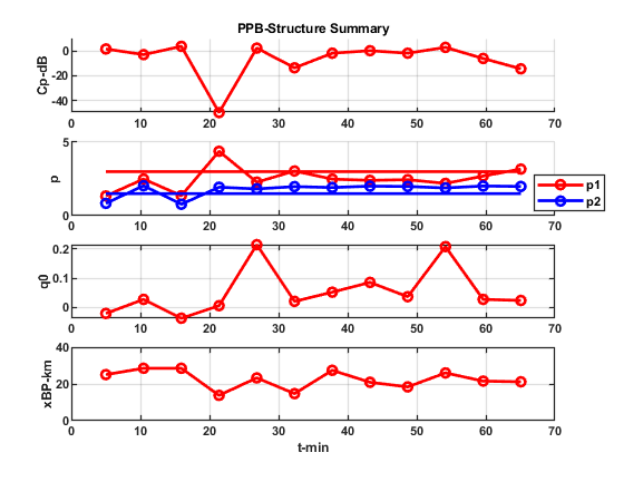


Figure 6: Summary of measured PPB structure parameters. Straignt line blue and red indicate initiate true values.

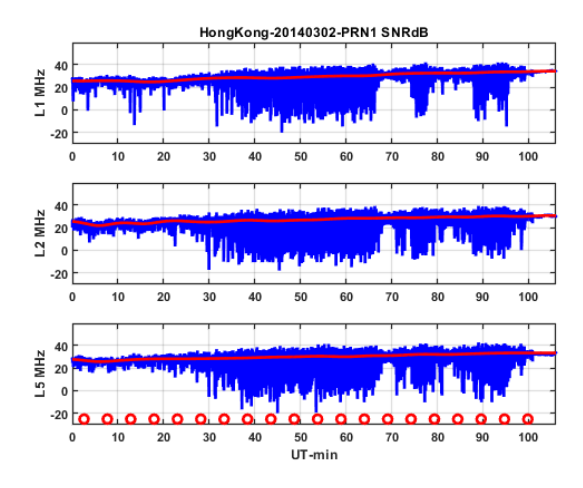


Figure 7: Representative example of Hong Kong intensity in SNR units (blue) with mean intensities overlaid (red). Red circles mark 5-min segments.

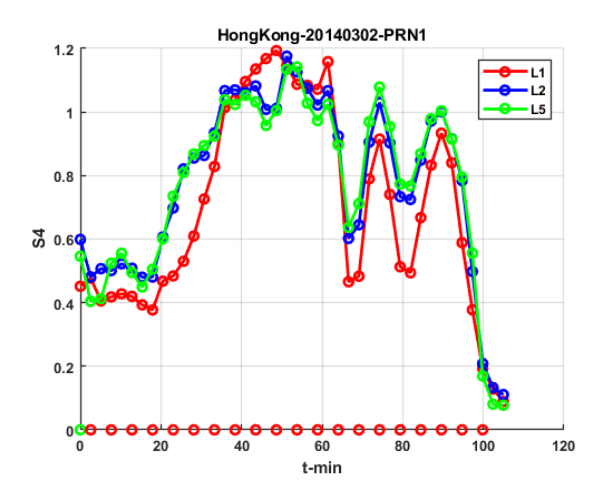


Figure 8: Summary of Hong Kong S4 from intensity data summarized in Figure 7

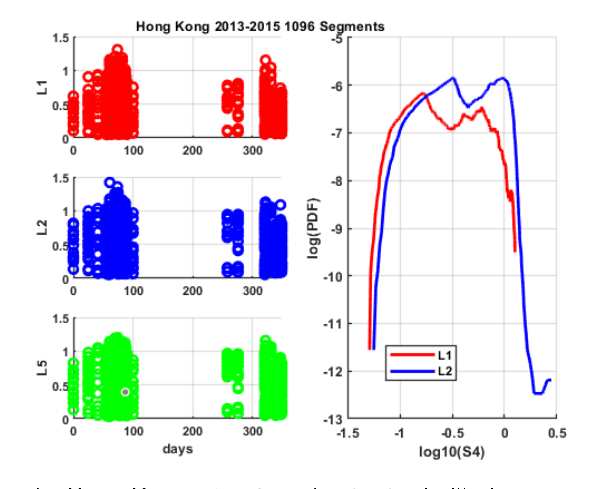


Figure 9: Left frames summarize the Hong Kong L1, L2, and L5 S4 scintillation occurrence. The right frame shows the L1 and  $L2 \log 10(S4)$  probablity distributions.

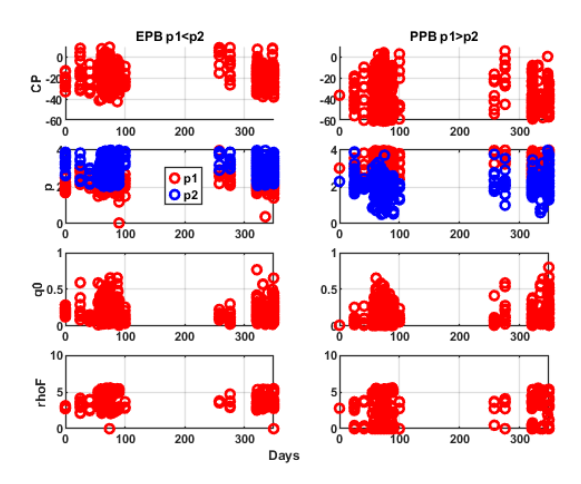


Figure 10: Hong Kong BP-IPE parameter summaries. Left frames summarize 504 EPB segments. Right frames summarize 544 PPB segments.

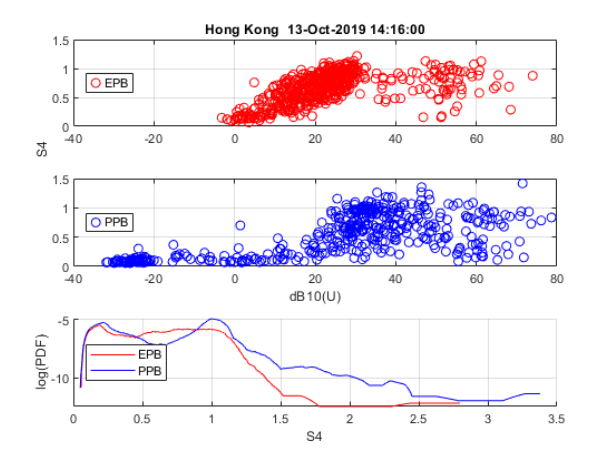


Figure 11: Upper frames show S4 versus U scatter diagrams EPB PPB segments as indicated. Lower frame shows corresponding S4 probability distributions.

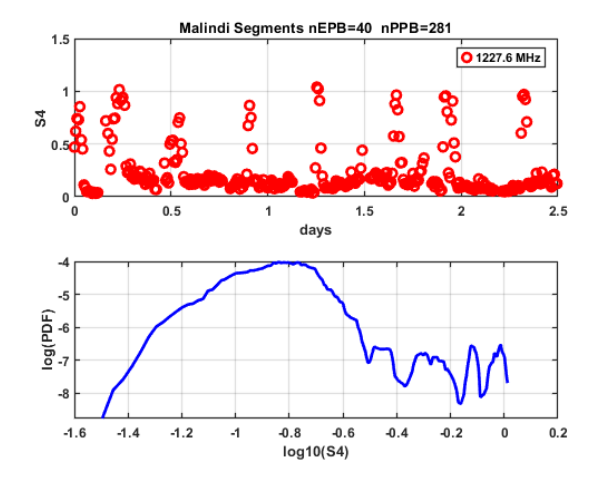


Figure 12: Intensity scintillation occurrence and S4 distribution from data recorded at Malindi 18-Mar-2019 20:45:02.

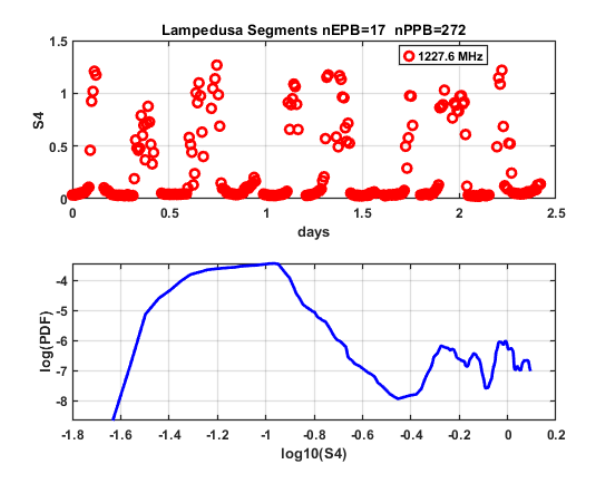
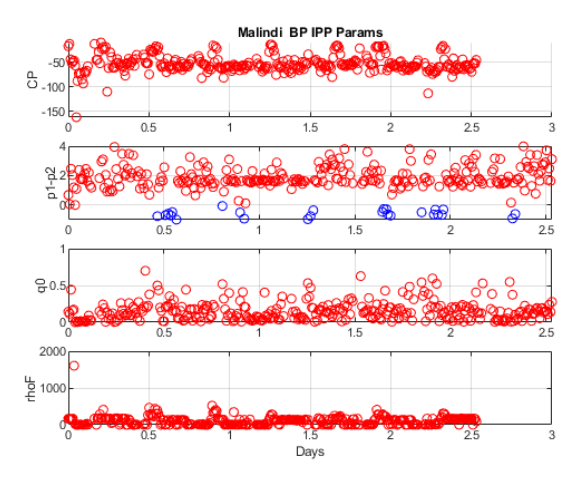
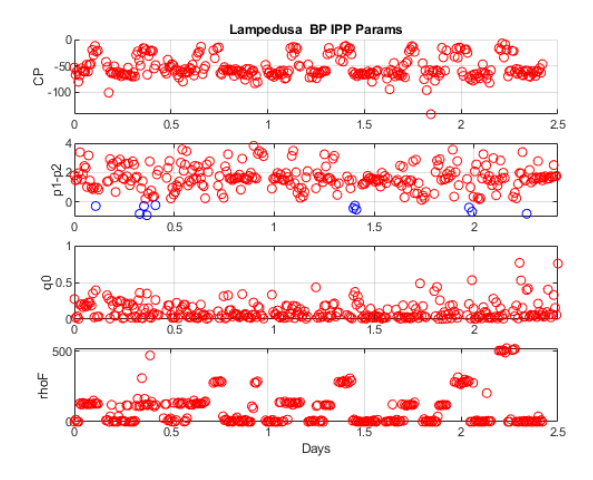


Figure 13: Intensity scintillation occurrence and S4 distribution from data recorded at Lampedusa 10-May-2019 16:00:00.



**Figure 14**: BP-IPP parameters from Malandi data. The second frame shows p1 - p2 with positive values identified as PPB signatures.



**Figure 15**: BP-IPP parameters from Lampedusa data. The second frame shows p1 - p2 with positive values identified as PPB signatures.

# References

282

290

291

292

293

294

295

296

297

298

299 300

301

302

- [1] C. Rino, C. Carrano, D. Vasylyev, T. Beach, B. Breitsch, Y. Morton, and K. Groves. On phase screen models for scintillation diagnostics.

  Radio Science, 60:e2024RS008204, 2025. https://doi.org/10.1029/2024RS008204.
- [2] C. Rino, C. Carrano, K. Groves, and T. Yokoyama. A configuration space model for intermediate-scale ionospheric structure. *Radio Science*, 53:1472–1480, 2018. https://doi.org/10.1029/2018RS006678.
- [3] K. B. Deshpande, G. S. Bust, C. R. Clauer, C. L. Rino, and C. S. Carrano. Satellite-beacon Ionospheric-scintillation Global Model of the upper Atmosphere (SIGMA) I: High-latitude sensitivity study of the model parameters. *J. Geophys. Res. Space Physics*, 119:4026–4043, 2014. https://doi.org/10.1002/2013JA019699.
  - [4] E. Costa, E. R. de Paula, L. F. C. Rezende, K. M. Groves, P. A. Roddy, E. V. Dao, and M. C. Kelley. Equatorial scintillation calculations based on coherent scatter radar and C/NOFS data. *Radio Science*, 46:RS2011, 2011. https://doi.org/10.1029/2010RS004435.
  - [5] C. Rino, B. Briestch, Y. Morton, Y. Jiao, D. Xu, and C. Carrano. A compact multifrequency GNSS scintillation model. *Institute of Navigation Journal*, 65:563–569, 2018. https://doi.org/10.1002/navi.263.
  - [6] C. S. Carrano, C. L. Rino, and K. M. Groves. Maximum likelihood estimation of phase screen parameters from ionospheric scintillation spectra. 15th International Ionospheric Effects Symposium, Alexandria, VA, May 9-11, pages 1–11, 2017.
  - [7] L. C. Lee. Wave propagation in a random medium: A complete set of the moment equations with different wavenumbers. *J. Math. Phys.*, 15:1431–1435, 1974. https://doi.org/10.1063/1.1666828.
  - [8] D. Xu, Y. T. J. Morton, C. L. Rino, C. S. Carrano, and Y. Jiao. A two-parameter multifrequency gps signal simulator for strong equatorial ionospheric scintillation: modeling and parameter characterization. *Navigation*, 67:181–195, 2019. https://doi.org/10.1002/navi. 350
  - [9] C. Rino, Y. Morton, B. Breitsch, and C. Carrano. Stochastic TEC structure characterization. J. Geophys. Res. Space Physics, 124:10571–10579, 2019. https://doi.org/10.1029/2019JA026958.
- [10] V. Ludwig-Barbosa, J. Rasch, T. Sievert, A. Carlström, M. I. Pettersson, V. T. Vu, and J. Christensen. Detection and localization of f-layer ionospheric irregularities with the back-propagation method along the radio occultation ray path. *Atmospheric Measurement Technology*, 16:1849–1864, 2023. https://doi.org/10.5194/amt-16-1849-2023.
- [11] B. Breitsch, Y. T. Morton, C. Rino, and D. Xu. GNSS carrier phase cycle slips due to diffractive ionosphere scintillation simulation
   and characterization. *IEEE Trans. Aerospace and Electronic Systems*, 56:3632–3644, 2020. https://doi.org/10.1109/TAES.2020.
   2979025.
- [12] C. L. Rino and C. S. Carrano. On the characterization of intermediate-scale ionospheric structure. *Radio Science*, 53:1316–1327, 2018. https://doi.org/10.1029/2018RS006709.
- [13] D. M. Olsson and L. S. Nelson. The Nelder-Mead simplex procedure for function minimization. TECHNOMETRICS, 17:45–51, 1975.
- 112 [14] C. S. Carmo, C. M. Denardini, C. A. O. B. Figueiredo, L. C. A. Resende, G. A. S. Picanço, P. F. Barbosa Neto, P. A. B. Nogueira, J. Moro, and S. S. Chen. Evaluation of different methods for calculating the ROTI index over the Brazilian sector. *Radio Science*, 56:e2020RS007140, 2020. https://doi.org/10.1029/2020RS007140.
- [15] C. Carrano and C. Rino. A theory of scintillation for two-component power law irregularity spectra: Overview and numerical results. *Radio Science*, 51:789–813, 2016. https://doi.org/10.1002/2015RS005903.
- 1317 [16] E. Pica, L. Spogli, C. Cesaroni, L. Alfonsi, H. Haralambous, F. Vallianatos, G. De Franceschi, V. Romano, and C. Marcocci. Assessing
  the ionospheric scintillations occurrence on L-band in the southern Mediterranean sector. *Adv. Space Res.*, 75:837–855, 2025. https:
  //doi.org/10.1016/j.asr.2024.10.032.
- 1320 [17] C. Cesaroni, M. Pezzopane, E. Zuccheretti, E. Pica, L. Spogli, D. Okoh, A. Pignalberi, J. Olwendo, L. Alfonsi, C. Marcocci, V. Romano,
  1321 R. Imam, G. De Franceschi, B. Nava, J. B. Habarulema, G. Santilli, A. Di Cecco, and J. Munzer. Establishing the first ionospheric observatory
  1322 in kenya: Early results from the norisk project. Adv. Space Res., 75:4698–4713, 2025. https://doi.org/10.1016/j.asr.2025.01.051.
- 1323 [18] B. Bougard, J. M. Sleewaegen, L. Spogli, S. V. Veettil, and J. F. Monico. CIGALA: Challenging the solar maximum in Brazil with Polarxs.

  1324 Proceedings of the 24th international technical meeting of the satellite division of the institute of navigation (ion GNSS 2011), pages 2572 –

  1325 2579, 2011.
- [19] L. Spogli, T. Alberti, P. Bagiacchi, L. Cafarella, C. Cesaroni, G. Cianchini, I. Coco, D. Di Mauro D, R. Ghidoni, F. Giannattasio, A. Ippolito,
  C. Marcocci, M. Pezzopane, E. Pica, A. Pignalberi, L. Perrone, V. Romano, D. Sabbagh, C. Scotto, S. Spadoni, R. Tozzi, and Ma.
  Viola. The effects of the May 2024 Mothers Day superstorm over the Mediterranean sector. *Annals Of Geophysics*, 67:PA218, 2024.
  https://doi.org/10.4401/ag-9117.
- [20] C. L. Rino, R. T. Tsunoda, J. Petriceks, R. C. Livingston, M. C. Kelley, and K. D. Baker. Simultaneous rocket-borne beacon and in situ measurements of equatorial spread F Intermediate wavelength results. *J. Geophys. Res. Space Physics*, 86:2411–2420, 1981. https://doi.org/10.1029/JA086iA04p02411.
- [21] S. Sa. B. Basu, J. P. McClure, W. B. Hanson, and H. E. Whitney. High resolution topside in situ data of electron densities and VHF/GHZ scintillations in the equatorial region. *J. Geophys. Res. Space Physics*, 88:403–415, 1983. https://doi.org/10.1029/JA088iA01p00403.
- [22] C. L. Rino, C. S. Carrano, and P. Roddy. Wavelet-based analysis and power law classification of C/NOFS high-resolution electron density data. *Radio Science*, 49:680–688, 2014. https://doi.org/10.1002/2013RS005272.
- [23] H. D. Craft and L. H. Westerlund. Scintillation at 4 and 6 GHZ caused by the ionosphere. AIAA 10th Aerospace Sciences Meeting, San Diego, CA, 72-179:1–6, 1972. https://doi.org/10.2514/6.1972-179.
- [24] S. J. Franke, C. H. Liu, and D. J. Fang. Multifrequency study of ionospheric scintillation at Ascension Island. *Radio Science*, 19:695–706,
   1984. https://doi.org/10.1029/RS019i003p00695.
- T. Yokoyama. A review on the numerical simulation of equatorial plasma bubbles toward scintillation evaluation and forecasting. *Prog. Earth Planet Sci.*, 4(37), 2017. https://doi.org/10.1186/s40645-017-0153-6.
- [26] C. Rino, T. Yokoyama, and C. Carrano. A three dimensional stochastic structure model derived from high resolution isolated equatorial plasma bubble simulations. *Earth, Planets and Space*, 75(64), 2023. https://doi.org/10.1186/s40623-023-01823-6.

5	[27]	C. Rino, Y. Morton, B. Breitsch, and C. Carrano. Stochastic TEC Structure Characterization. J. Geophys. Res. Space Physics, 124:10571-10579, 2019. https://doi.org/10.1029/2019JA026958.